ADVANCED MATERIALS
www.advmat.de

2D Co-Mo-Hydroxide-Based Multifunctional Material for the Development of H_2-Based Clean Energy Technologies

Daniel Muñoz-Gil, Celia Castillo-Blas, Dawid Krystian Feler, Isabel Gómez-Recio, Miguel Tinoco, Ana Querejeta-Fernández, Rodrigo González-Prieto, Felipe Gándara, Romualdo Santos Silva Jr, Pilar Ferrer, Carlos Prieto, Luc Lajaunie, José Luis Martinez-Peña, María Luisa Ruiz-González,* and José María González-Calbet**

Layered double hydroxides (LDH) based on transition metals are highly flexible in tailoring their dimensionality, lattice, and electronic structures, making them promising candidates as multifunctional 2D materials for the development of clean energy technologies and boosting the use of hydrogen as an energy vector. In this paper, strategic anion substitution in cobalt LDH is an appealing strategy to produce a material with two-fold functionality, electrochemical and magnetocaloric response, offering a sustainable alternative to existing electrocatalysts and cryogenic refrigerants. It is unambiguously demonstrated that (poly)oxomolybdate-based specimens interleave in Co LDH nanosheets up to a Co:Mo = 1:0.4 ratio, leading to an interstratified material. This intercalation greatly benefits the kinetics of the oxygen evolution reaction for H_2 production, boosting the catalytic sites due to the expansion of the interlayer space, induced by the bulky molybdates which also partially modify the Co oxidation state of αCo(OH)$_2$ nanolayers, favoring charge transfer. In parallel, the interleaved Mo species strengthen superexchange interactions compared with pristine α-Co(OH)$_2$, effectively adjusting the operating temperature toward the liquid hydrogen range (2030 K). This specific temperature range allows to fill a critical gap in magnetocaloric materials, as few systems can simultaneously achieve both large magnetic entropy changes and structural stability.

1. Introduction

Reduction of the emissions derived from the combustion of fossil fuels through the incorporation of efficient renewable energies is a major concern of our society. In this landscape, hydrogen is a unique energy vector with a prominent role toward the reduction of carbon emissions as it exhibits the highest gravimetric energy density of any energy carrier, and its combustion generates only water. Nowadays, the use of green hydrogen, obtained from water electrolysis, represents one of the most promising clean alternatives to current energy sources. However, some important challenges must first be addressed to industrially produce green hydrogen viably. One of the key features required to scale up the production of green hydrogen is related to the improvement of the kinetics of the involved half-reactions, which is particularly sluggish for the oxygen evolution reaction (OER) since four electrons must be transferred to produce

D. Muñoz-Gil, D. K. Feler, I. Gómez-Recio, M. Tinoco, A. Querejeta-Fernández, R. González-Prieto, M. L. Ruiz-González, J. M. González-Calbet
Departamento de Química Inorgánica
Facultad de Ciencias Químicas
Universidad Complutense de Madrid
Madrid 28040, Spain
E-mail: luisarg@ucm.es; jgcalbet@ucm.es

The ORCID identification number(s) for the author(s) of this article can be found under https://doi.org/10.1002/adma.202512458

DOI: 10.1002/adma.202512458

C. Castillo-Blas, F. Gándara, R. S. Silva Jr, C. Prieto, J. L. Martinez-Peña
Instituto de Ciencia de Materiales de Madrid (ICMM)
Consejo Superior de Investigaciones Científicas (CSIC)
Madrid 28049, Spain
E-mail: martinez@icmm.csic.es

R. S. Silva Jr
Departamento de Física de Materiales
Facultad Ciencias Físicas
Universidad Complutense de Madrid
Madrid 28040, Spain

P. Ferrer
Diamond Light Source, Diamond House
Didcot OX11 0DE, UK

L. Lajaunie
Departamento de Ciencia de los Materiales e Ingeniería Metalúrgica y Química Inorgánica
Facultad de Ciencias
Universidad de Cádiz
Puerto Real 11510, Spain

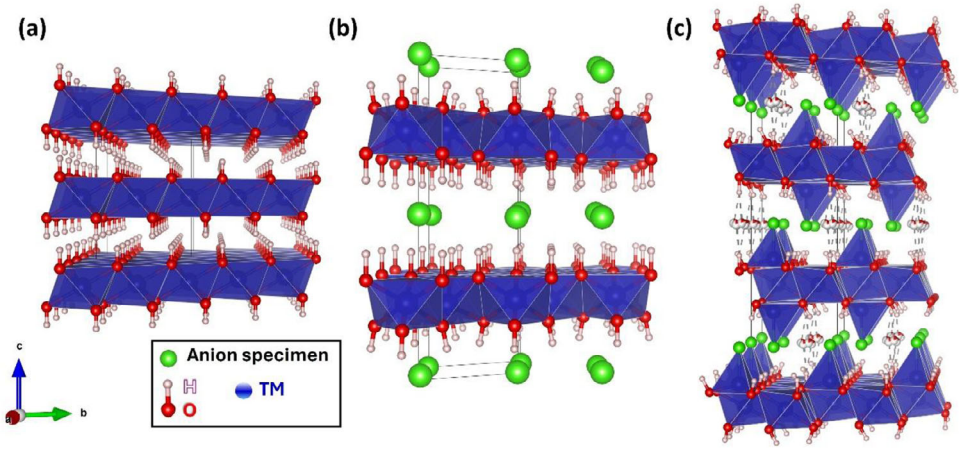

Figure 1. Schematic representation of the structural types: a) Brucite; b) Hydrotalcite, and c) Simonkolleite.

O_2. Nowadays, RuO_2 and IrO_2 oxides are considered the best catalysts for this evolution reaction as a consequence of their lowest potential at useful current densities. However, their high cost and scarcity strongly limit their use in large-scale applications. In addition, another challenge related to green hydrogen-based technologies is associated with the safe and economically efficient transport and storage of H_2. Some options are currently explored, but one of the most examined is liquid hydrogen. Nevertheless, H_2 liquefaction is a high-cost process and, conventionally, not environmentally friendly.[1] Hence, substitutes for these methods are gaining growing interest. Among them, the development of magnetic refrigeration exploiting the magnetocaloric effect (MCE) appearing on certain materials is stepping up as a potential alternative to current liquefaction methods. The MCE is based on the isothermal change of magnetic entropy (ΔS_M) upon applying or removing an external magnetic field to specific magnetic materials.[2,3] Therefore, magnetocaloric materials undergo temperature changes under an applied magnetic field enabling them to reach the temperatures required for the H_2 liquefaction. This effect is environmentally friendly, as it does not require the use of harmful gases, and is more effective than conventional methods.[4] So far, materials containing rare-earth elements are the most promising candidates for this effect because of their large magnetic moments.[3,5,6] Nevertheless, due to the scarcity, criticality, and high cost of these resources, the search for alternative MCE materials is rather urgent.

According to the above ideas, optimizing both hydrogen-related technologies, water splitting and H_2 liquefaction, requires the development of more active OER electrocatalysts and more efficient MCE materials, respectively. Concerning OER optimization, the substitution of noble metals by cheaper and abundant transition metals (TM) of the first row, 3d, has been a widely employed strategy. In the case of MCE materials, in the last years there has been growing interest in finding TM-based alternatives because of the limiting factors surrounding the use of rare-earth elements. The development of new 2D nanostructures of transition metal oxides (TMO) plays a fundamental role for boosting catalytic activities. This is due to the vast increment in active sites compared to standard 3D materials, since, in this 2D limit, most of the atoms are at the surface, the quantum confinement modifies their electronic configuration, and the electronic conductivity usually increases. Specifically, layered compounds based on layered double hydroxide (LDH) and oxyhydroxides have been extensively studied to optimize their OER performance. They offer flexible lamellar structures built from $[TM(OH)_6]$ octahedral unities sharing edges, characteristic of the brucite and hydrotalcite structural types. In the brucite lattice, $TM^{II}(OH)_2$, the layers are neutral and the apical hydroxyl groups point to the interlayer space (≈4.6 Å) (**Figure 1a**). In hydrotalcite-like phases (Figure 1b), $TM_{1-x}{}^{II}TM_x{}^{III}(OH)_2.nH_2O$, the positively charged layers, due to the coexistence of divalent and trivalent cations, are compensated by intermediate anions. This leads to an increase of the interlayer spacing (7–8 Å) compared to the brucite type. Among LDH, the Co-related family stands out as one of the most promising to propel OER in alkaline media.[7] $Co(OH)_2$ crystallizes in two polymorphs, α and β. β-$Co(OH)_2$ form is brucite-like (Figure 1a), while α-$Co(OH)_2$ exhibits the so-called simonkolleite structure type (Figure 1c),[8,9] which also incorporates anions, X, in the lamellar space, $Co^{II}(OH)_{2-y}X_{2y}.nH_2O$ (X = anion). In this type, only Co^{2+} cations are present and, in order to keep the electroneutrality, the additional anions partially substitute several OH^- groups. As a result, a portion of the Co^{2+} cations is tetrahedrally coordinated above and below the octahedral layers[9,10] resulting, again, in an expanded[11] lamellar structure. Therefore, the incorporated anions are bonded to cobalt, completing their tetrahedral environment with hydroxyl anions. As a consequence of the expansion of the interlayer space, electrochemical performance is enhanced since charge and mass diffusion are improved, which facilitates access of reactants to the active sites.

Furthermore, the key role of the tetrahedral sites in the electrochemical properties of α-$Co(OH)_2$ has been highlighted, as it exhibits superior OER activity compared to the β polymorph[12,13] and to the Co-Al expanded hydrotalcite phase, which only has octahedral sites.[11] It is then clear that the Co hydroxide system offers multiple possibilities to optimize its electrochemical behavior, boosting the number active sites since it encompasses the ability of tuning: the i) number of layers, through controlled soft chemistry approaches, ii) interlayer space, modifying or adding specimens into the interlayer space and iii) electronic and crystal

environment of Co, through the modification of both anionic and cationic sublattices.

Taking into account the first point, that is, the number of layers, obtaining 2D or ultrathin Co-based LDH nanostructures is an effective way to increase their surface-to-volume ratio allowing to improve α-$Co(OH)_2$ OER activity. This goal can be achieved by liquid-phase processes operating at low temperature, such as treating a cobalt salt in a basic medium, and using a directing agent.[14–17] Second, the use of different cobalt salt precursors such as chlorides, carbonates, nitrates, or acetates leads to hydroxides with different intercalated anions, Cl^-, CO_3^{2-}, NO_3^-, and CH_3COO^-.[18] Even though they are all expanded phases, their interlayer spaces are similar, ≈8 Å. This space can be more effectively increased if bulky specimens are introduced. In this sense, it has been recently reported that the incorporation of more complex inorganic salts as polyoxometallates allows a significant increase in interlayer space and modulation of electron transfer, improving the electrochemical behavior of the material.[19,20]

Despite the important role of the above-mentioned points affecting the materials surface, the structural and electronic environments of Co are also critical aspects to optimize α-$Co(OH)_2$ catalytic activity. It is well known that pristine α-$Co(OH)_2$ nanosheets can be oxidized to γ-CoOOH nanophase, with a rather similar layered structure, in which Co^{3+} cations are in a distorted octahedral environment displaying the e_g^1 configuration.[15,21] It is widely recognized that the occupation of the e_g orbitals plays a fundamental role in OER/ORR processes. Specifically, an effective binding between the TM and adsorbate specimen requires an e_g orbital occupation close to "one" electron, that is, e_g^1[22] in such a way that the interaction between both specimens is neither too strong nor too weak, according to the Sabatier Principle. On the other hand, substituting Co by other cations like Fe can activate the initially inactive Co^{2+}octahedral sites, boosting the overall electrocatalytic activity of α-$Co(OH)_2$.[23] Besides, Density Functional Theory calculations suggest that doping with high valence metals like W(VI), Mo(VI), and Cr(VI) can modulate the electronic structure of Co and other 3d TM, providing optimal absorption energies for OER intermediates.[24] Although e_g^0 occupancy is considered not adequate for an optimum adsorption of OH* groups, empty orbitals can accept electron density from cobalt by modifying its electronic configuration, which may lead to an improvement of the material's catalytic activity. Furthermore, it should be noticed that such a substitution also contributes to the increase of the covalent nature of the M—O bond which favors electron transfer, as well as the participation of the oxygen sublattice in the catalytic process. This situation can be understood considering the approximation of the O p band to the Fermi level, facilitating the overlapping of the O p and TM d bands. Subsequently, the electron transfer O→TM enables the formation of $(O_2)^{n-}$ specimens, whose decomposition releases O_2.[25] Even more, the surface reconstruction of the electrocatalyst plays a critical role in generating surface active sites and boosting the surface reaction. In this sense, Bai et al.[26] have demonstrated through real-time XPS studies that molybdenum-substituted CoO presents faster surface reconstruction kinetics and best OER activity in comparison to the parent oxide. In the last years, there have been different approaches to introduce Mo in nanostructured 2D Co hydroxides and oxyhydroxides, all leading to improvements in the OER electrochemical response. Nevertheless, the reported information about the location and distribution of Mo in the original Co matrix is controversial.[16,27–29] Considering the high tendency of Mo to adopt high oxidation states, the most plausible situation would be its stabilization as oxometallates negatively charged in the interlayer space. This situation would also promote layer separation. In fact, Vaysse et al. reported bulk Ni—Co based double hydroxide with intercalated oxometallates, $(M_2O_7)^{2-}$ inferred from X-ray diffraction (XRD), Fourier transform infrared spectroscopy (FTIR), and extended X-ray absorption fine structure studies.[30] On the other hand, Davantès et al.[30] studied the sorption of (poly)molybdate ions into double hydroxides with Zn^{2+} and Al^{3+} cations, showing its high affinity for heptamolybdate ($Mo_7O_{24}^{6-}$) species and its preferential sorption in comparison with MoO_4^{2-} ions or other protonated polymolybdate species.[31] Nevertheless, no electrochemical characterization was reported in these last two publications. Considering the above description of Co-related LDH, the nanostructuration linked to the inclusion of high valence cations is a promising strategy to improve their OER activity. Regardless of the demonstrated beneficial effect of high valence TM, such as Mo and W, to promote the OER activity of Co hydroxides and oxyhydroxides, studies devoted to unveil its real location remain scarce, hindering the proposal of a catalytic mechanism.

Regarding the magnetic properties of Co hydroxides, most available data focus on the β-$Co(OH)_2$ system, with limited studies on α-$Co(OH)_2$. However, both phases share common magnetic features, primarily strong in-plane (inter-layer) ferromagnetic (FM) interactions mediated by the Co—OH—Co superexchange pathway, which forms a crystallographic angle close to 90° in both cases. Slight variations in this angle lead to differences in interaction strength and, consequently, in the FM ordering temperature (T_C), though a clear FM order within the $[Co(OH)_6]$ layers persists. Additionally, a much weaker interplanar (inter-layer) magnetic interaction exists, which can be either FM or antiferromagnetic (AFM), depending on the interlayer distance. This AFM exchange interaction could rise to AFM coupling between layers at low temperatures, if the layer distances can overcome the dipolar FM interaction between them. The FM dipolar interaction is strongly reduced with distance. Our primary interest lies in studying the magnetic properties of the LDH sample containing Mo, but we also aim to compare its magnetic behavior with the Mo-free α-$Co(OH)_2$ to better understand the Co sublattice's magnetic order in each case. If metallate Mo specimens are intercalated in the lamellar space of the Co LDH, changes in the magnetic behavior could be observed since the interactions between layers are sensitive to their separating distance. Moreover, a giant MCE has been recently reported in the related Co LDH $Co_4(OH)_6(SO_4)_2[enH_2]$,[32] in which the excellent magnetocaloric properties are attributed to a second-order ferromagnetic phase transition with 10 K < T_c < 15 K. Furthermore, the layered character of the structure seems to play a central role in this behavior, leading to easy-plane magnetic anisotropy with XY spins that can easily be aligned in small magnetic fields, with a corresponding large magnetic entropy change and minimal hysteresis on removing or reversing the field.[32] Therefore, we have proceeded to study the MCE in the molybdenum compound since it exhibits an expanded layered structure.

Our approach to face these problems, efficient OER and MCE, is to employ the same material based on a 2D Co-related hydroxide interleaved with a Mo oxometallate. For that purpose, it is mandatory to shed light on the compositional, structural, and electronic characterization of Co LDH nanosheets containing Mo, in comparison to α-$Co(OH)_2$, through a battery of diffractometric and spectroscopic techniques which will provide not only average but also local information. To properly study short-range order phenomena in these complex interstratified Co hydroxides, the pair distribution function (PDF) analysis is a highly valuable tool to unveil the occupancy of the space between Co layers through the investigation of the Mo—O and metal–metal correlations of the possible (poly)oxomolybdate species. Transmission electron microscopy (TEM) and associated spectroscopic techniques will also provide a direct identification of the layered morphology as well as infer the Co and Mo location. Moreover, considering the intriguing and versatile magnetic behavior of these layered systems, which is strongly dependent on the layer separation,[33,34] we have also performed a complete magnetic characterization of the Co LDH sample containing molybdenum as well as the α-$Co(OH)_2$. Exploiting the morphological, structural, magnetic, and electronic features that expanded 2D Co-LDH can exhibit, the aim of this paper is to carefully analyze the possible intercalation and interaction of Mo (poly)oxometallates within the Co hydroxide layered matrix, obtained by a simple one-pot synthesis, to study its multifunctional behavior according to their electrochemical and magnetic properties. This study opens new prospects for the development of functional materials based on (poly)oxomolybdates interleaved in Co LDH to generate and store green H_2 from water-splitting and its following liquefaction.

2. Results and Discussion

Our work represents a significant advance in the study of novel multifunctional interstratified polyoxometallates based on molybdenum species incorporated in cobalt LDH synthesized in a one-pot synthesis. We will mainly focus on the study of a sample resulting from the introduction of Mo in pristine α-$Co(OH)_2$ with a nominal Co: Mo = 1:0.4 ratio. This Mo-containing sample will be designated as Co-Mo-1/0.4 LDH and will be always compared with the pristine α-$Co(OH)_2$. Their functional behavior, both electrochemical and magnetocaloric, is studied based on careful compositional and structural characterization. Samples with intermediate lower Mo content Co-Mo-1/0.1 LDH and Co-Mo-1/0.25 LDH will also be used to better understand the evolution of the structural features as a function of the Mo incorporation. For higher Mo content the α-$Co(OH)_2$ type is not maintained.

The XRD pattern corresponding to Co-Mo-1/0.4 LDH is very similar to that of the layered α-$Co(OH)_2$ simonkolleite type ($R\bar{3}$ m) characteristic of the Mo free sample, as observed in Figure S1 (Supporting Information). It is worth highlighting the displacement of the (00l) reflections, corresponding to the interlayer distance, toward lower angles in the (Co-Mo-1/0.4 LDH) sample. This fact indicates an enlargement of the interlayer distance, that is, $d_{(003)}$ = 9.9 Å for (Co-Mo-1/0.4 LDH) vs 7.8 Å in α-$Co(OH)_2$, suggesting the incorporation of bulkier species such as (poly)oxomolybdates. For lower Mo contents, Co-Mo-1/0.1 LDH and Co-Mo-1/0.25 LDH, the (003) reflection appears at intermediate 2θ angles between that of the Mo-free sample and that of the sample with the highest Mo (Co: Mo = 1/0.4) content (Figure S1, Supporting Information) which means an increase of the corresponding d_{003} periodicity. Furthermore, changes in reflection width and intensity are appreciable as Mo content increases, suggesting changes on the pristine simonkolleite phase. This information has been further investigated by the high-resolution PXRD of the Co-Mo-1/0.4 LDH collected at ID15A (ESRF). Pawley refinement performed with the corresponding pattern indicates a decrease in the symmetry for this material, likely due to an elongation between layers. This strongly supports the hypothesis of the position of the (poly)oxomolybdates in the interlayer space (**Figure 2**, Table S1, Supporting Information).

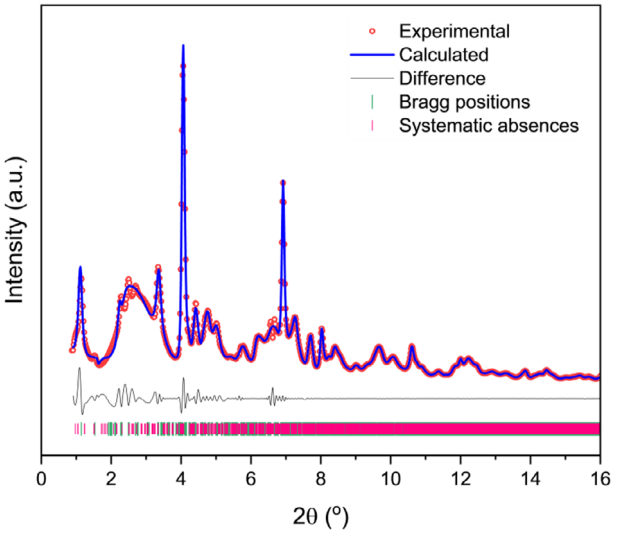

Figure 2. Experimental (red circles) and calculated (blue continuous line) XRD Pawley refinement of Co-Mo-1/0.4 LDH. λ = 0.18972 Å. The vertical green bars indicate the positions of the Bragg peaks, and the grey line at the bottom is the difference between the experimental and calculated patterns.

Average cationic analysis by electron probe microanalysis (EPMA) agrees with the incorporation of Mo according to the nominal composition (Table S2, Supporting Information). Following previous publications,[20] the compositional analysis reflects the presence of chlorine in the α-$Co(OH)_2$ pristine sample, while its disappearance in Co-Mo-1/0.4 LDH can be attributed to chlorine substitution by (poly)oxometallate species in the interlayered space. This complements the successful interlayer introduction of molybdenum inferred from diffraction data. Additionally, FTIR spectra supply valuable information about the nature of the bonds in each compound. The spectrum of the raw α-$Co(OH)_2$ (Figure S2a, Supporting Information) exhibits a broad and intense band centered ≈3400 cm^{-1}, characteristic of the O—H stretching vibrations of interlayered water and H-bound OH groups. The band centered ≈1600 cm^{-1} is attributed to the bending mode of water molecules. Similar features are observed in the Co-Mo-1/0.4 LDH compound (Figure S2a, Supporting Information), but with noticeably less intensity. Furthermore, an intense band ≈3600 cm^{-1} also appears. This band can be assigned to the O—H stretching mode of the free Co—OH groups,

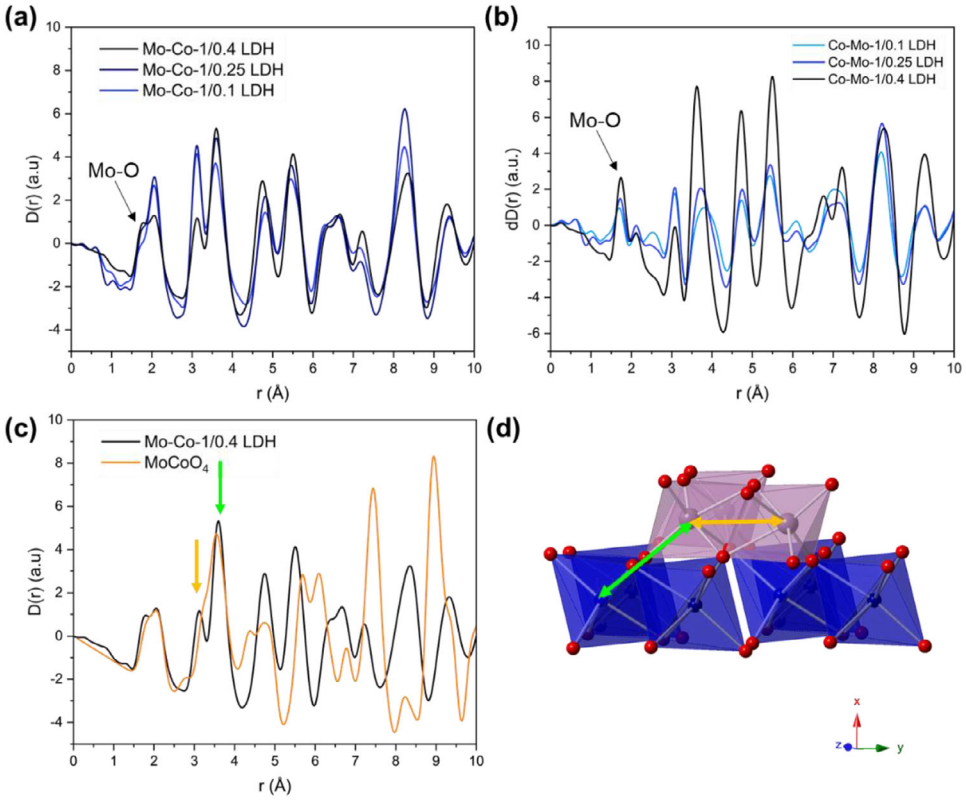

Figure 3. a) D(r)s of the materials that incorporate different amounts of Mo species. b) dPDF of all the materials that incorporate different amounts of Mo species. c) Comparison of the calculated $CoMoO_4$ oxide and the experimental Mo-Co-1/0.4 LDH, showing very similar correlations at short-range order for both materials. d) Depiction of MoO_6 species connected via corner-sharing to the Co-layer showing the Co–Mo (green) and Mo–Mo (yellow) correlations. Color atoms: Cobalt (blue), Molybdenum (violet), Oxygen (red). Hydrogens were omitted for clarity.

characteristic of β-$Co(OH)_2$, indicative of very weak or absent H bonding.[35] This band, together with the intensity decrease of the broad band at ≈3400 cm^{-1}, evidences different structural features with respect to the starting Mo free hydroxide. Another distinction comes from the signals below 1000 cm^{-1}, which are associated with M—O vibration bands. These vibrations are modified in the Co-Mo-1/0.4 LDH compound because of the appearance of a sharp peak centered at 850 cm^{-1} compatible with Mo—O stretching in Na_2MoO_4 and $(NH_4)_6Mo_7O_{24}$ specimens (Figure S2b, Supporting Information).

The ensemble of the above XRD, FTIR, and EPMA data allows us to propose that even when the Co-Mo-1/0.4 LDH sample has been prepared using the same conditions that α-$Co(OH)_2$, the introduction of Mo metallates seems to be favored against chloride at the interlayered space, in agreement with the increase of this space observed by XRD. Nevertheless, it is also important to emphasize the high diffuse component observed in all the above XRD patterns, especially as the Mo content increases, reaching it maximum in Co-Mo-1/0.4 LDH. Such a situation reflects short-range ordering phenomena, which could also be related to the presence of randomly distributed (poly)oxomolybdates between the Co hydroxide layers. This leads to a poor atom correlation that could be understood due to the lower Mo proportion against Co. To address this situation, it is necessary to use methods that provide information about the local atomic environment and the relative positions of the near-neighbor atoms. Therefore, X-ray total scattering experiments were performed to investigate and confirm the Mo—O and metal–metal correlations of the polyoxomolybdate species to get more precise structural information of the local occupancy between $Co(OH)_2$ layers. The measured I(Q) patterns (Figure S3, Supporting Information) were processed using established procedures to extract the structure factor, S(Q) (Figure S4, Supporting Information), and the PDF, D(r). In this case, we used D(r) to accentuate medium and long-range correlations (**Figure 3**; Figure S5, Supporting Information). To better interpret features observed in the D(r)s patterns, partial PDFs of the α-$Co(OH)_2$ and β-$Co(OH)_2$ phases were studied (Figure S6, Supporting Information). The main short-range order correlations in α-$Co(OH)_2$ were assigned following previous reported structures (Figure S7, Supporting Information). Upon comparison with samples containing incorporated Mo, additional correlations clearly appear, increasing with the amount of Mo incorporated. These new correlations also showed a trend within the increment of the Co/Mo ratio (Figure 3a). Particularly, the correlation located at 1.77 Å, often assigned to Mo—O distances, was found to have higher intensity with a higher amount of Mo incorporated. This strongly suggests that the incorporated Mo species remain consistent across different Co/Mo ratios. To further isolate these correlations, differential PDFs (dPDFs) were calculated for all the modified materials. This method, previously applied to unveil polyoxometallate incorporation in various materials[36] consists in the subtraction of the PDFs of the modified materials

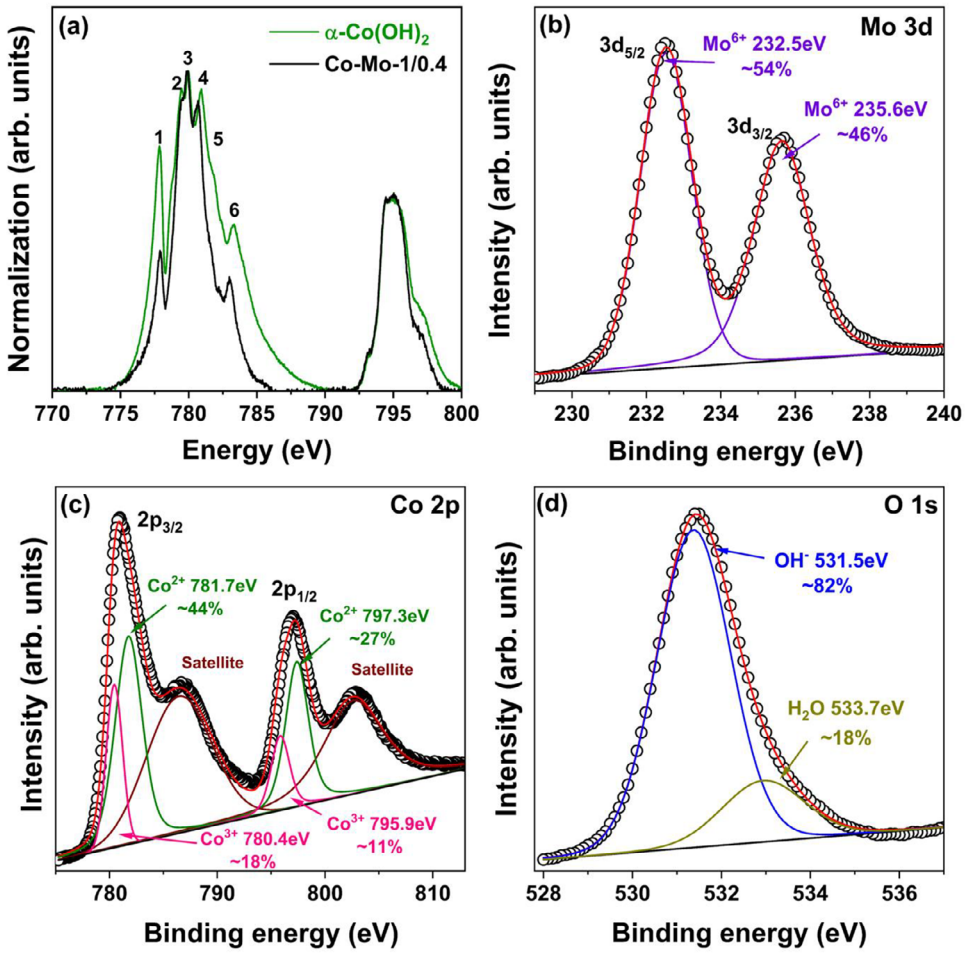

Figure 4. a) Co-L edge XAS spectra of α-Co(OH)$_2$ and Co-Mo-1/0.4 LDH samples (2p1/2 and 2p3/2 after subtraction of normalized jump); b) Mo 3d spectrum of Co-Mo-1/0.4 DLH; c) Co 2p XPS spectrum of Co-Mo-1/0.4 LDH; d) O 1s XPS spectrum of Co-Mo-1/0.4 LDH.

over the α-Co(OH)$_2$, applying a scale factor to minimize the Co—O correlation (Figure 3b). The resulting dPDFs revealed seven main correlations located at 1.75, 3.08, 3.62, 4.72, 5.50, 8.24, and 9.26 Å, indicating that the incorporated species in the interlayered space must account these correlations. A great number of multiple polyoxomolybdates and molybdenum oxides were evaluated to match the intensities of these new correlations. The strong 1.75 Å correlation, from the Mo—O, is especially significant given that Mo comprises less than 50% of the total metal content. This suggests a predominance of Mo—O distances ≈1.75–1.77 Å. According to literature, Mo—O bond lengths can range from 1.77 Å (terminal) to 2.1 Å (bridging), indicating the likely presence of MoO_6 octahedra sharing vertices or edges.[37] Therefore, likely Mo octahedral sharing one or two vertex or edges would satisfy the ratio 1.77 and 2.1 distance. Among the structures evaluated, $CoMoO_4$ (ICSD: 281 235) emerged as a promising candidate, exhibiting Mo—Mo and Co—Mo distances of 3.1 and 3.62 Å, respectively (Figure 3c; Figure S8, Supporting Information). These findings support the hypothesis that the incorporated molybdate species consist of edge-sharing MoO_6 octahedra, connected to the Co hydroxide layers via corner-sharing coordination (Figure 3d). However, a definitive structural model cannot yet be proposed, and further analysis would be required to fully resolve the structure of the modified materials.

To gain insight into the electronic structure of Co in these samples, X-ray absorption (XAS) experiments were performed at the Co L-edges. For comparison, **Figure 4a** displays the signal obtained for the L_3 and L_2 lines after normalization to the edge jump for the undoped α-Co(OH)$_2$ and the Co-Mo-1/0.4 LDH samples. First, the structure and comparison of L_3 and L_2 lines with those of CoO show that Co^{2+} is the main oxidation state. Furthermore, as reported by Bora et al. for β-Co(OH)$_2$[38] the L_3 line is formed by 6 sub-peaks. The multiple peaks 1, 2, and 3 originate from the electronic transition associated with the octahedral symmetry of the Co^{2+} site. Similarly, as in CoO and β-Co(OH)$_2$, their presence (shown in Figure 4) allows us to establish that cobalt is located mainly in octahedral positions. Further information can be obtained by calculating the $L_{3,2}$-ratio between the intensities of L_3 and L_2 absorptions lines, $R_{L3,2} = I(L_3)/I(L_2)$, as well as the so-called branching-ratio, $R_{br} = I(L_3)/(I(L_3) + I(L_2))$.[39] Thus, lower values of the $R_{L3,2}$-ratio are associated to lower electron occupancy in d orbitals that may be used to obtain information of the average oxidation state. Additionally, higher values of the branching ratio indicate a greater presence of high-spin states.

Table S3 (Supporting Information) summarizes the $R_{L3,2}$- and R_{br}-ratios reported for CoO and β-$Co(OH)_2$, taken as reference compounds, and those obtained for α-$Co(OH)_2$ and Co-Mo-1/0.4 LDH samples. The $R_{L3,2}$- ratio obtained in our samples is lower than that of CoO, in agreement with the presence of Co^{3+}. Moreover, when compared to that in α-$Co(OH)_2$, in coincidence with the very slight energy shift of peak 1 (≈0.15 eV), the observed decrease in the $R_{L3,2}$- ratio in the Co-Mo-1/0.4 LDH sample is consistent with an increase in the average oxidation state of cobalt. On the other hand, α-$Co(OH)_2$ and Co-Mo-1/0.4 LDH samples have very similar R_{br}-values between them being lower than that of CoO and slightly higher than that of α-$Co(OH)_2$, indicating less high-spin states than CoO, also in agreement with the below obtained magnetic moment of Co (μ_{eff} ($Co(OH)_2$:Mo) = 3.67 μ_B/Co) compared to that in CoO (μ_{eff} (CoO) = 3.98 μ_B/Co).[40]

To gain deeper insight into the oxidation states, X-ray photoemission spectroscopy (XPS) analyses were conducted. The whole XPS spectra corresponding to Co-Mo-1/0.4 LDH shows peaks corresponding to C 1s, O 1s, Mo 3d, and Co 2p (Figure S9, Supporting Information). The XPS of Mo 3d core level doublet, located at 232.5 and 235.6 eV (Figure 4b), can be well fitted to two Gaussians which precisely correspond to molybdenum (VI), as previously reported.[27,41,42] On the other hand, Co 2p signals have been fitted to two doubles and their corresponding satellites (Figure 4c): the signals attributed to Co^{2+} (781.7 and 797.3 eV); and two less intense maxima located at 780.4 and 795.9 eV, which agree with already reported values from Co^{3+}.[27,43–46] The relative proportion of cobalt oxidation states has been estimated: 72% of cobalt stays as Co^{2+}, while the remaining 28% is Co^{3+}. Hence, the approximate average oxidation state of cobalt measured by XPS is +2.28, which is in good agreement with the XAS results, that detected partial oxidation of Co. Last, the XPS 1s oxygen signal has also been analyzed (Figure 4d). That signal can be deconvoluted into two distinctive Gaussians. The lesser contribution (18% of the area), appearing at 533.7 eV, can be attributed to absorbed H_2O.[27,47–49] On the contrary, a curve peaking at 531.5 eV is the major contributor to the oxygen 1s signal (82% of the area below the maximum), which can be ascribed to OH^- species.[27,47–49] The XPS result confirms the hydroxide nature of the sample, the presence of molybdenum in the +6 oxidation state, and the partial oxidation of cobalt.

Scanning electron microscopy (SEM) characterization was employed to unveil particle morphology and homogeneity. The SEM images contained in Figure S10a (Supporting Information) reveal a plate-like morphology for the α-$Co(OH)_2$ phase, in agreement with previous literature. This general appearance is maintained in the Co-Mo-1/0.4 LDH sample (Figure S10b, Supporting Information). Nevertheless, a remarkable decrease in the lateral dimensions of these platelets can be noticed, which provokes their random orientation (Figure S10c, Supporting Information).

To gain further knowledge about the nature of these Co-Mo-1/0.4 LDH platelets as well as deeper structural information, a TEM study was performed. Low magnification TEM evidences their ultrathin or 2D nature (**Figure 5**a,b), as happens in the parent α-$Co(OH)_2$ compound (Figure S11a, Supporting Information). However, a notable difference regarding the lateral layer dimensions can be appreciated, as suggested in the previous SEM study. The α-$Co(OH)_2$ phase exhibits higher lateral dimensions (see detailed description in Supporting Information) causing the bending and/or folding of the layers making possible to distinguish individual layers (Figure S11a,b, Supporting Information), along the perpendicular direction. In Co-Mo-1/0.4 LDH, the flat layers exhibit much smaller dimensions, ≈20 nm (Figure 5a,b), compared to the several microns of the undoped Co phase.

Furthermore, bending is not observed at the edges (Figure 5a). This phenomenon can be explained based on the reduction in the particle size, which may decrease the stress in the platelets. Besides this fact, two orientations can be distinguished by: i) platelets of the so-called flat layers, previously mentioned, viewed along the [001] zone axis, and ii) elongated particles, perpendicularly oriented. On the other hand, the particle size reduction can also be responsible for the absence of particles preferentially orientated along [001], that is, in the direction parallel to the layers. Instead, they are indistinctly distributed on the TEM grid along this direction, [001], and the perpendicular one, [100], in agreement with the previous SEM images. From the particles oriented perpendicular to the basal plane, an average thickness of 3.8 nm, corresponding to ≈4 layers, can be estimated (Figure S12, Supporting Information). HRTEM images of the flat layers, in both Co and Co–Mo compounds, show that they are built by small particles in which the measured periodicities as well as the corresponding FFT agree with the [001] orientation (Figure 5b,c). The presence of holes in between particles reflects the ultrathin nature of the layers. HRTEM images corresponding to the [001] orientation show an interlayer periodicity of 0.98 nm, evidencing the increase of this distance in the samples containing Mo according to XRD information (Figure 5d), supporting the incorporation of Mo oxometallates between the octahedral Co layers. The high instability of these samples under electron beam irradiation should be emphasized, which is due to the presence of labile specimens containing hydrogen, which can be easily released, leading to the shrinking of the lattice after ≈60 s.

The local compositional study by means of EDS confirms the presence of Co and Mo in Co-Mo-1/0.4 LDH (Figure S13 Supporting Information). In comparison with α-$Co(OH)_2$ the absence of chlorine in Co-Mo-1/0.4 becomes clear (Figure S11g, Supporting Information), in agreement to EPMA.

A STEM-HAADF-EELS study was performed in the Co-Mo-1/0.4 LDH sample to get information about the Co and Mo distribution and their oxidation state. Low magnification STEM-HAADF image reflects again the ultrathin nature of the samples (**Figure 6**a).

A characteristic atomic resolved STEM-HAADF image along [001] zone axis is shown in Figure 6b, while the expanded distance between layers can be identified in the high-resolution STEM-HAADF image in Figure 6c. The brightest contrast of the limiting edges should be noticed, while the intensity decreases inside these limits. It can be proposed that the brightest contrast corresponds to the hydroxide Co layers while the lower intensity, between them, would be related to Mo metallates. This situation could result apparently incoherent according to the higher atomic number of Mo (Z = 42) in comparison to Co (Z = 27). Nevertheless, it is worth remembering that the Mo percentage is quite low compared to Co (Co: Mo = 1:0.4). Unfortunately, the sample instability hinders the acquisition of atomically resolved images. Despite these problems, the spectrum-image acquisition over areas [100] of oriented particles (Figure 6d–f) suggests that Mo could be interleaved with the Co layers. A representative area

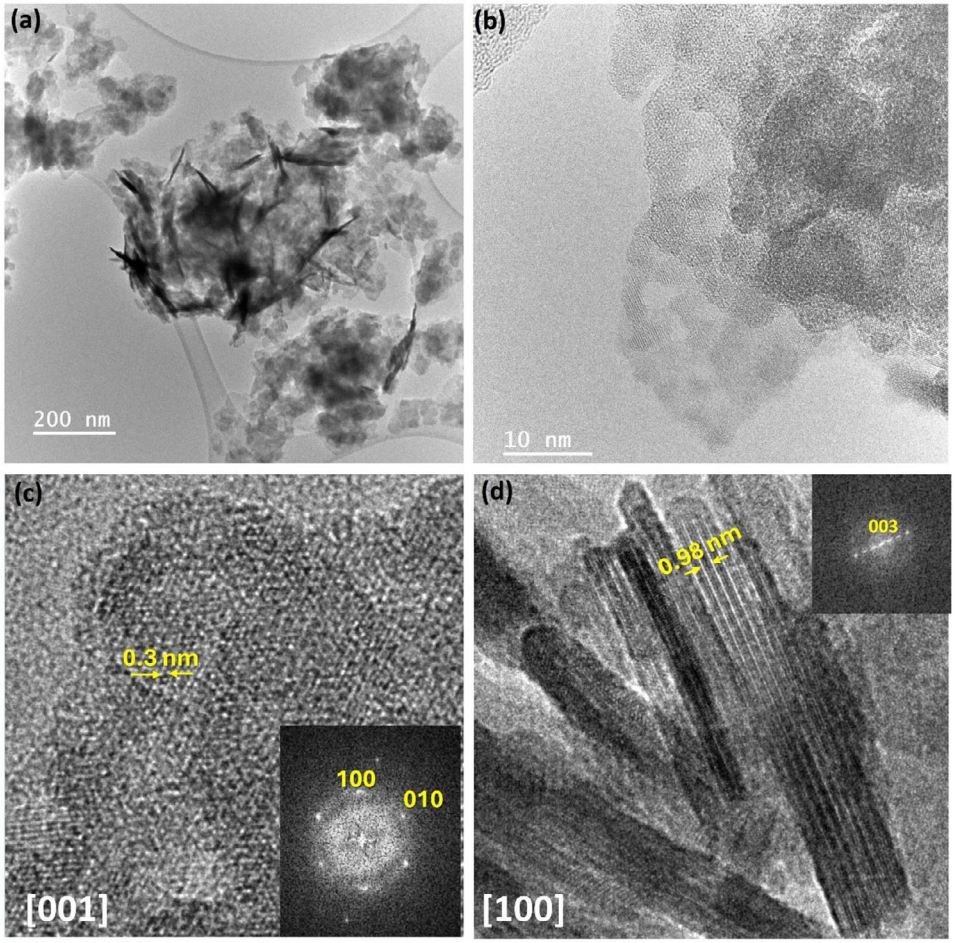

Figure 5. TEM images of Co-Mo-1/0.4 LDH sample. a) Low magnification image; b) higher magnification image where the ultrathin nature of the nanoparticles is evidenced; c,d) HRTEM images acquired along the [001] and [100] zone axes, respectively. The increase of the d_{003} distance, as compared to that of α-$Co(OH)_2$, is outlined in (d).

for this study is outlined in green in Figure 6d. The corresponding chemical maps for Co and Mo are shown in Figure 6e. These maps have been obtained after subtraction from the EELS sum spectra (Figure 6e) simultaneously acquired with scanning across the area marked in green. The sum spectrum (Figure 6e) shows the energy edge onsets for Mo–$M_{2,3}$, O–K, and Co–$L_{2,3}$.

An analysis of the fine structure of Co-$L_{2,3}$ and Mo-$M_{2,3}$ was carried out to gather information about the oxidation states of cobalt and molybdenum at a local level. Line-scans evidence the homogeneous presence of Co and Mo in all the particles. The average oxidation states of Co gathered from different line scans are 2.3 ± 0.1. This indicates the presence of ≈30% of Co^{3+}, in agreement with the energy shift observed in the XAS spectra and XPS. A typical example is shown in Figure S14 (Supporting Information). Similarly, the Mo oxidation state was estimated from EELS by calculating the Mo M_3/M_2 intensity ratio, following a methodology detailed elsewhere.[50] A representative example is shown in Figure S15 (Supporting Information). Ratios were determined from several areas and compared to those obtained on MoO_3 and MoO_2 reference samples, which were acquired under identical experimental conditions. The measured M_3/M_2 ratios were 1.82 for the Co-Mo-1/0.4 LDH sample, and 1.88 and 2.11 for the MoO_3 and MoO_2 references, respectively. These results are in good agreement with previously reported values for the reference compounds,[50] and confirm the presence of Mo(VI) in the sample. The slightly lower M_3/M_2 ratio observed for the sample may be attributed to differences in electronic structure and the potential influence of noise in the EELS signal.

The ensemble of these compositional and structural data allows proposing that Mo (poly)oxometallates have been intercalated in the lamellar space of α-$Co(OH)_2$. PDF reveals that edge-sharing MoO_6 octahedra are sharing corners with Co hydroxide layers. Regarding the electronic structure, different spectroscopic techniques indicate the coexistence of Co (II) and Co(III) in the $Co(OH)_2$ layers, while the most probable situation for the interstratified Mo is Mo (VI).

Once the Co-Mo-1/0.4 LDH sample has been structurally and electronically characterized, its functionality was tested starting by analyzing its electrochemical and magnetic behavior. Regarding the electrochemical characterization, **Figure** 7a compares the OER results obtained for the Mo-samples and the undoped material. Reference data for OER (RuO_2) electrodes, as well as for the Vulcan mesoporous carbon support are also included. It can be clearly noted that all samples display significantly better OER

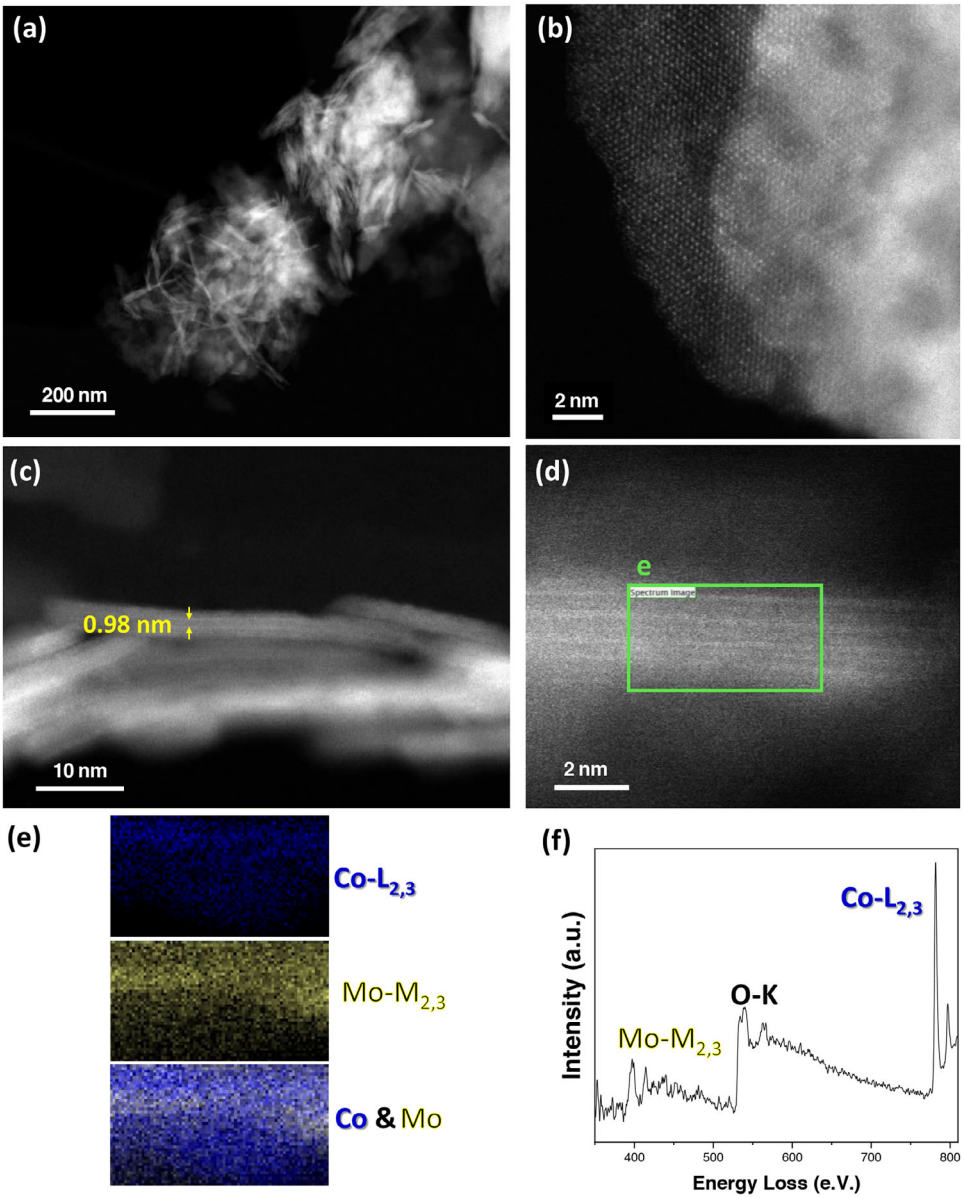

Figure 6. STEM-HAADF-EELS analyses of Co-Mo-1/0.4 LDH sample. a) Low magnification HAADF image showing the ultrathin nature of the Mo doped sample; b) Atomic-resolved STEM-HAADF image along [100]; c) High resolution STEM-HAADF evidencing the layered microstructure; d) 2D particle in which the EELS spectra has been simultaneously acquired, with the HAADF image, across the marked area in green; e) Chemical maps, from top to bottom: Co (blue), Mo (yellow) and the corresponding mixture. f) Sum spectra of the green area.

performances than the Vulcan carbon support. Apart from that, the pristine Co hydroxide underperforms when compared to the reference RuO_2 oxide in OER. However, the voltammograms indicate that the OER activity significantly increases with the Mo content within the whole current density range. The enhancement in electrochemical performance upon the incorporation of Mo into the system has been recently reported.[27,51] However, these studies do not clarify the specific role of Mo in the OER process, the atomic Co/Mo ratio, or the precise location of Mo within the layered hydroxide structure.[27,51] As shown in Figure 7a, the incorporation of Mo into $Co(OH)_2$ markedly enhances the onset potential for the OER, lowering it to 1.47 V in both the Co-Mo-1/0.1 LDH and Co-Mo-1/0.4 LDH samples, compared to 1.60 V observed for the undoped material. This enhancement can be attributed to electronic structure modulation since Mo incorporation alters the electronic density of states near the Fermi level, creating sites with modified oxidation states and coordination environments that serve as more active sites for the adsorption of OER intermediates (*OH, *O, *OOH).[52,53] PDF analysis further indicates that Mo atoms coordinate with oxygen within the octahedral sheets, strengthening the covalent character of the Mo—O—Co bond and enhancing charge transfer efficiency. This improved electronic interaction reduces the energy barrier associated with each electron transfer step, thereby accelerating the

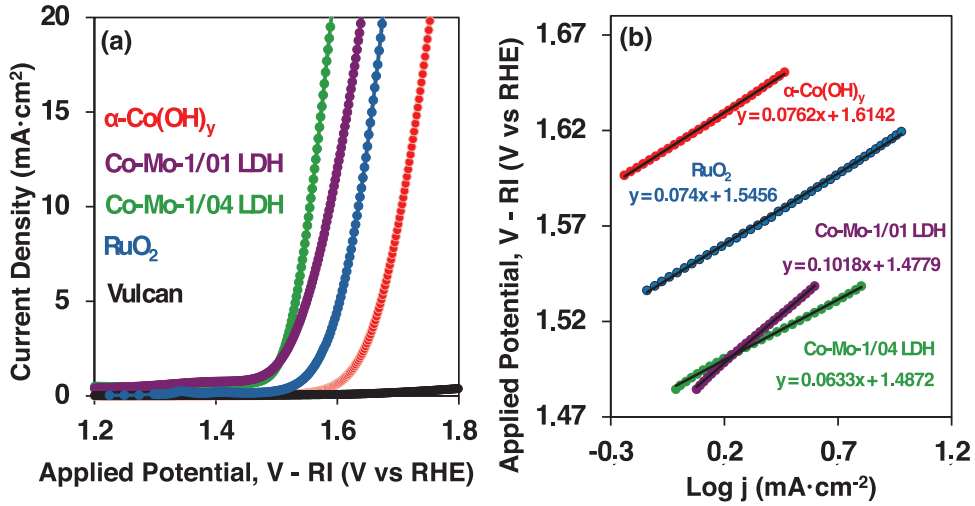

Figure 7. a) Linear scanning voltammogram obtained at 1600 rpm comparing the OER activity of the pristine α-$Co(OH)_2$ (red line), Co-Mo-1/0.1 LDH (purple line) and Co-Mo-1/0.4 DLH (green line) samples. b) Tafel plots based on data from Figure 7a comparing the OER activity of the of the pristine α-$Co(OH)_2$ (red line), Co-Mo-1/0.1 LDH (purple line) and Co-Mo-1/0.4 LDH(green line) samples. Data for conventional 20% Platinum/Carbon and RuO_2 fresh catalysts are also included as a reference.

overall reaction kinetics. In addition, the incorporation of anionic Mo species partially promotes the oxidation of Co^{2+} to Co^{3+}, as evidenced by XAS, XPS, and EELS results. This oxidation state transition enhances OER activity by yielding an e_g orbital occupancy close to one electron, which is known to be optimal for OER catalytic performance.[22] Comparing Co-Mo-1/0.1 LDH and Co-Mo-1/0.4 LDH, differences in Tafel slopes[54] are observed despite similar onset potentials (see Figure 7b). This can be related to morphology-dependent effects induced by the higher Mo content (Figure S16, Supporting Information). The Co-Mo-1/0.4 LDH sample exhibits thinner, less aggregated nanosheets, resulting in a larger electrochemically active surface area and a higher density of active sites.[55] According to these authors, in situ Mo etching selectively thins and exfoliates the nanosheets, producing ultrathin, less stacked structures that enhance mass transport and reaction kinetics, thereby reducing the Tafel slope.[55] Consequently, as evidenced by the low-magnification TEM images in Figure S16 (Supporting Information), the textural differences between the Co-Mo-1/0.1 LDH and Co-Mo-1/0.4 LDH samples could account for the lower Tafel slope in the latter.

Regarding the magnetic properties, **Figure 8a** shows the temperature dependence of the *dc* magnetic susceptibility $\chi(T)$ for Co-Mo-1/0.4 LDH, together with the inverse magnetic susceptibility $\chi^{-1}(T)$. First, we observe an increase in magnetic susceptibility (from 1.2 to 4.8 emu mol^{-1} Oe) at low temperatures compared to α-$Co(OH)_2$ (Figure S17, Supporting Information). Two distinct magnetic anomalies are observed, which are clearly confirmed by the derivative of the magnetic susceptibility (Figure S18a, Supporting Information). The first negative anomaly is related to the susceptibility upturn associated with the FM order of the Co ions in the $Co(OH)_4$ layers, with $T_C = 11.4$ K, whereas the second (positive) anomaly at lower temperature is related to the AFM ordering of the 2D Co layers ($T_N = 2.8$ K), separated by the (poly)oxomolybdates. Clearly, the T_C is shifted to a lower temperature compared to α-$Co(OH)_2$ ($T_C = 39.6$ K). On the other hand, the second anomaly is very similar than a pure system with $T_N = 2.6$ K (Figure S18b, Supporting Information). From electron microscopy measurements, the interlayer distance expands from 8 Å in the pristine compound to ≈10 Å in the Co-Mo-1/0.4 LDH system. Previous studies suggest that 10 Å marks the threshold distance at which AFM coupling weakens significantly compared to FM dipolar interactions.[32] Strikingly, the in-plane FM ordering temperature (T_C) of the Co layer is three times higher in the undoped material (39.4 K), than in the Mo-doped analog (11.4 K). This substantial enhancement, promoted by the inclusion of molybdenum-based (poly)oxometallates, likely stems from structural distortions in the $Co(OH)_6$ octahedra, as Co-Mo-1/0.4 LDH exhibits a pronounced deviation of the Co–O–Co superexchange angle from 90° closer to 180°, thereby disrupting the magnetic exchange pathways. Consequently, the altered orbital overlap near 180° significantly suppresses the in-plane superexchange interactions between Co ions. This distortion, along with the increased exchange angle, weakens the FM coupling in the Co-Mo-1/0.4 LDH system, ultimately reducing its T_C by a ≈3.5 factor compared to the pristine compound.

The $\chi^{-1}(T)$ curve was fitted by the modified Curie–Weiss (C–W) law $\chi(T) = \chi_0 + C/(T-\Theta)$, where χ_0 is a temperature-independent susceptibility, C is the Curie constant, and Θ is the Weiss temperature.[56] The fit gave $\Theta = 18.6$ K, $\chi_0 = 5.48 \times 10^{-2}$ emu mol^{-1}, and an effective paramagnetic moment of $\mu_{eff} = 3.67$ μ_B/Co. The positive Θ-value indicates a predominance of FM interactions. In contrast, the similar fit for α-$Co(OH)_2$ (see inset in Figure S17, Supporting Information) yielded a Θ-value of −79.1 K and an effective magnetic moment of 3.87 μ_B/Co. The negative Θ value suggests that the interactions are mainly AFM. Clearly in this second case, the Mo free compound, the curvature of the inverse susceptibility changes very much in the same temperature range indicating more complex magnetic interactions. For the Co-Mo-1/0.4 LDH system, we expect to have mostly Co(II) and Mo(VI); however, the XAS, XPS, and EELS analysis showed that Co exhibits +2.3 average oxidation state. Therefore, we can assume that Mo is

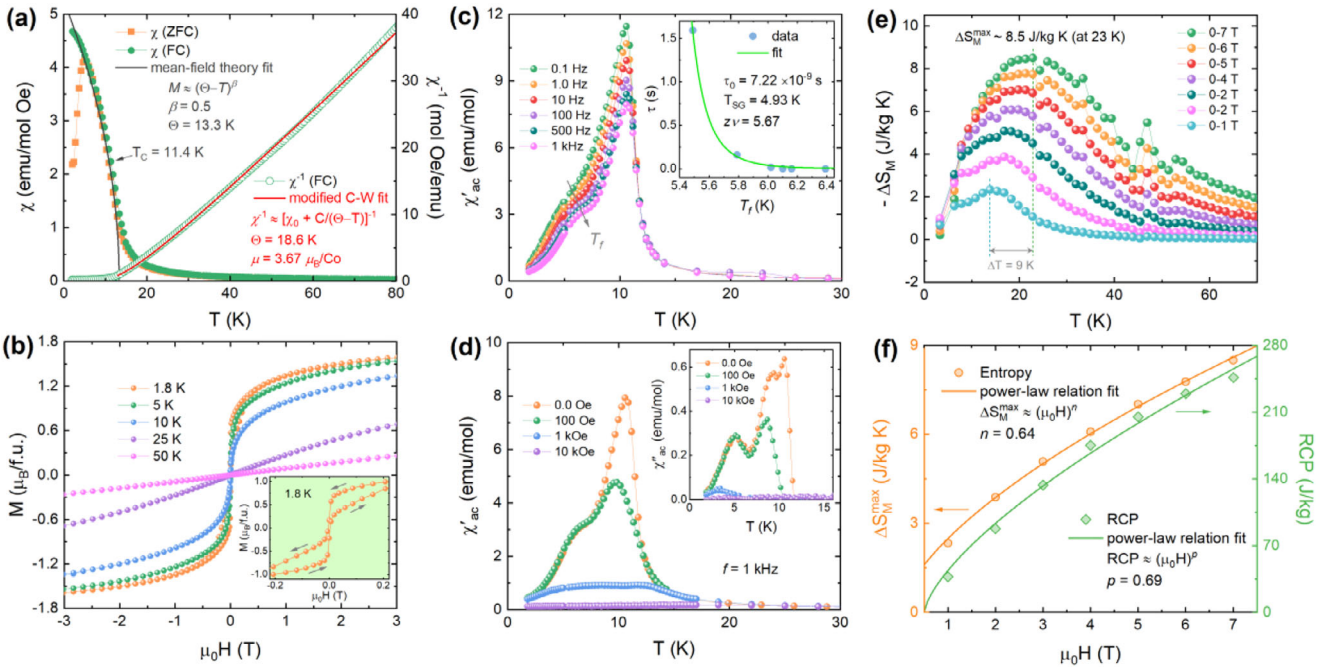

Figure 8. Magnetic characterization of Co-Mo-1/0.4 LDH sample. a) Temperature dependence of magnetic susceptibility χ, recorded in the ZFC/FC modes under $\mu_0 H_{dc} = 0.1$ T and inverse susceptibility $\chi^{-1}(T)$, together with the mean-field theory fit and modified C–W fit, respectively. b) Isothermal M(μ_0H) curves at different temperatures. Insets show a zoom of the curve at 1.8 K. c) Temperature dependence of the real part of *ac* magnetic susceptibility χ'_{ac}. The inset shows the $\tau(T_f)$ data relation, that the fit gives τ_0, T_{SG}, and $z\nu$ values. d) Temperature-dependent χ'_{ac} at different fixed *dc* magnetic fields, and the imaginary part χ''_{ac} for the same *dc* magnetic fields is shown in the inset. e) Extracted magnetic entropy change plotted against temperature for magnetic field changes in the range of 0.5–7 T. f) ΔS_M^{max} and RCP as function of $\mu_0 H$ together with their respective power-law fits.

diamagnetic ($4d^0$) and Co is present as a $0.7Co^{2+} + 0.3Co^{3+}$ ratio, in which the paramagnetic moment in the high-spin state for Co(II) ($S = 3/2$) is 3.87 μ_B and 4.9 μ_B for Co(III) ($S = 2$).[57] Consequently, the calculated effective paramagnetic moment for Co-Mo-1/0.4 LDH is 3.81 μ_B/Co, which is strikingly like the obtained one from the modified C–W law, as indicated above.

Figure 8b displays the $M(\mu_o H)$ isotherms at various temperatures for Co-Mo-1/0.4 LDH. At 1.8 K, the magnetization saturates at 1.7 μ_B/Co at 7 T. In low fields and low temperatures, the behavior is nearly linear, consistent with an AFM order state (see inset of Figure 8b). However, increasing the applied field induces a transition to a hysteresis loop resembling FM order, with a small coercive field (≈4.5 kOe). Above the Curie temperature ($T_C = 11.4$ K), the system exhibits paramagnetic behavior, with a sharp decline in the ordered moment between 1.8 K and T_C. Unlike the Mo-doped system, the parent compound (α-Co(OH)$_2$ exhibits a lower saturation magnetization of 0.8 μ_B/Co at 1.8 K and 7 T, whereas the hysteresis loop persists up to ≈21 kOe (Figure S19, Supporting Information). Associated to this, the effective magnetic moment per Co atom involved in the long-range magnetic ordering can be inferred from the $\chi \times T(T)$ plot, as presented in Figure S20 (Supporting Information) for both compounds. A significant rapid decrease of the effective moment to almost zero for $T < T_C$ is observed to Co-Mo-1/0.4 LDH, indicating that no net effective moment is available after the long-range magnetic order. Conversely, a slightly broader and less intense peak was revealed for α-Co(OH)$_2$, reflecting the observed difference in saturation magnetization between the compounds at 1.8 K. This supports the most FM character in the Co-Mo-1/0.4 LDH compound.

Given the complexity of the magnetic behavior, we supplemented our measurements with *ac* magnetic susceptibility studies across the same temperature range, in a broad frequency spectrum (0.1 Hz–1 kHz and magnetic amplitude of 1 Oe), and under varying *dc* external magnetic fields. As shown in Figure 8c, the real component of the *ac* susceptibility frequency-dependent $\chi'_{ac}(f)$ for Co-Mo-1/0.4 LDH exhibits a clear FM transition at $T_C = 11.4$ K. Above T_C, the χ'_{ac} data overlap perfectly with the frequency, whereas below T_C, however, χ'_{ac} displays pronounced frequency dependence, signaling a dynamic magnetic process in this temperature regime and suggests a complex dynamic of the expected FM domains with a close dynamic as that observed in the case of spin-glass behavior. This performance contrasts sharply with that of α-Co(OH)$_2$ (see Figure S21, Supporting Information), which χ' presents also a non-disperse character for T above T_C, but behaves differently below T_C. Instead, two peaks at 19 and 30 K below T_C are observed, that suggest competing FM interactions, potentially mediated by particle-size distribution or magnetic frustration. To provide quantitative analysis for Co-Mo-1/0.4 LDH, we performed the standard theory of dynamic scaling near the freezing temperature T_f for given excitation frequencies, in which the relaxation time $\tau = (2\pi f)^{-1}$ around the T_f is described by $\tau = \tau_0[T_f/T_{SG} - 1]^{-z\nu}$, where T_{SG} is the SG temperature (glass dynamic of the ferromagnetic domains) as the $f \to 0$, τ_0 is the characteristic flipping time of single spin flip, and $z\nu$ is the dynamical critical exponent.[46] The fit of $\tau(T_f)$ relation (inset of Figure 8c) yielded $\tau_0 = 7.22 \times 10^{-9}$ s, $T_{SG} = 4.93$ K, and $z\nu = 5.67$.

The obtained relaxation time τ_0 lies within the range characteristic of cluster SG (ferro-domains) systems (10^{-7}–10^{-11} s), contrasting with canonical spin glasses (10^{-12}–10^{-14} s),[46,58] where individual spins fluctuate faster. The slower spin dynamics observed in Co-Mo-1/0.4 LDH indicate the predominance of interacting spin clusters (domains) rather than isolated spins. This interpretation is further supported by the *zv*-value, which falls within the typical 4–13 range,[59] providing compelling evidence for the cluster SG behavior in this system. Furthermore, applying a moderate external *dc* field of 100 Oe (fixed frequency at 1 kHz), the T_C peak in χ'_{ac} is significantly reduced and the peak temperature slightly reduced, as displayed in Figure 8d. In contrast, the anomaly near T_N persists unchanged under fields up to 100 Oe. At higher fields (≥10 kOe), all anomalies disappear completely across the entire temperature range spanning both transitions (Figure 8d; Figure S22, Supporting Information). Specifically, a dual peak is observed around T_C in the imaginary part χ''_{ac} (see the inset of Figure 8d). However, like to χ'_{ac}, this peak is drastically suppressed for fields exceeding 100 Oe.

Relative to the MCE of both α-$Co(OH)_2$ and Co-Mo-1/0.4 LDH samples, isothermal magnetization curves $M(H)$, measured between 8 and 100 K at 3 K steps in temperature and field-ascending mode up to applied magnetic fields of 7 T, are shown in Figure S23a,b (Supporting Information). Typically, materials that undergo a second-order magnetic phase transition tend to exhibit negligible hysteresis near their transition temperature, which is particularly important for achieving high cooling efficiency in the thermodynamic cycle of a magnetic refrigeration system.[60] As demonstrated by the Arrott plots (H/M vs M^2) in Figure S23c,d (Supporting Information), these compounds undergo a second-order phase transition near the magnetic transition temperature. Thus, the magnetic entropy change (ΔS_M) can be indirectly obtained based on the Maxwell relations:[61]

$$-\Delta S_M = S_M(T,0) - S_M(T,H) = -\int_0^{H_{max}} \left[\frac{\partial M(T,H)}{\partial T}\right]_H dH \quad (1)$$

The extracted $-\Delta S_M(T)$ curves under selected magnetic fields (0–1 T ≤ ΔH ≤ 0–7 T) for Co-Mo-1/0.4 LDH compound are shown in Figure 8e. As expected, the peak related to MCE is centered around T_C. Notably, the pronounced peak reaches a maximum magnetic entropy change $-\Delta S_M^{max}$ of 8.5 J kg^{-1} K^{-1} at 23 K for 0–7 T field change, which was significantly shifted to lower temperature and enhanced compared to α-$Co(OH)_2$, that yields 4.7 J Kg^{-1} K^{-1} at 50 K (Figure S24, Supporting Information). This may be related to the increased angle of Co-OH-Co superexchange interactions arising from Mo introduction, which decreases T_C. Furthermore, a greater presence of Co^{3+} in this compound favors an increase in the measured magnetic moment (Figure S23, Supporting Information), resulting in enhanced MCE.

Figure 8f displays the $-\Delta S_M^{max}$ as function of $\mu_0 H$, which follows the power law $-\Delta S_M^{max} \approx (\Delta\mu_0 H)^n$. The fit gives the exponent n = 0.63(7), which corresponds to typical mean-field ferromagnets (n = 2/3). To fully assess the properties relevant for refrigerant applications, we examined the relative cooling power (RCP) parameter,[62] RCP = $|\Delta S_M^{max}| \times \Delta\delta T_{FWHM}$, where $\Delta\delta T_{FWHM}$ is the full width at half-maximum of $-\Delta S_M(T)$ curves. RCP reached a maximum of RCP^{max} = 246.4 J kg^{-1} at 0–7 T, which is comparable to some typical compounds such as $Gd_5Ge_2Si_2$ (240 J kg^{-1}),[63] $GdNi_4Si$ (322 J kg^{-1}),[64] and $TbCo_{1.9}Fe_{0.1}$ (271 J kg^{-1}).[65] Similarly to ΔS_M^{max}, RCP also follows a power law RCP $\approx (\Delta\mu_0 H)^p$ with an exponent p = 0.68(6) (Figure 8f).

To further contextualize the magnetocaloric performance of both α-$Co(OH)_2$ and Co-Mo-1/0.4 LDH compounds, we compare it with other similar reported prospective magnetocaloric materials. A table containing all the materials can be found in Table S4 (Supporting Information). Especially, we plotted the magnetic entropy change normalized by the applied magnetic field ($\Delta S_M/\mu_0 H$), as a function of the MCE peak temperature (T_{MCE}) (**Figure 9**). Clearly, the MCE of Co-Mo-1/0.4 LDH is lower than that of some notable intermetallic compounds such as $Er_{12}Co_7$[66] ($|\Delta S_M| \approx 18.3$ J kg^{-1} K^{-1} at 6.5 K), $HoCo_3B_2$[67] ($|\Delta S_M| \approx 14.4$ J kg^{-1} K^{-1} at 11.8 K), and $GdCoC_2$[68] ($|\Delta S_M| \approx 28.4$ J kg^{-1} K^{-1} at 15 K). However, these materials are costly due to the scary responsibility in the market of rare-earth elements. The hydroxides compounds $[Ni(C_4H_3O_4)_2(H_2O)_4]$[69] ($|\Delta S_M| \approx 11.2$ J kg^{-1} K^{-1} at 3.5 K) and $Co_4(OH)_6(SO_4)_2[enH_2]$[32] ($|\Delta S_M| \approx 21$ J kg^{-1} K^{-1} at 17 K) also demonstrate significant MCE in the liquid-hydrogen temperature range, highlighting the advantage of layered hydroxides in achieving tunable, anisotropic magnetic interactions. In that regard, the magnetocaloric response of our α-$Co(OH)_2$ and Co-Mo-1/0.4 LDH compounds places among the promising rare-earth-free candidates for hydrogen liquefaction (below 30 K), surpassing structurally related compounds like $(C_6H_5CH_2CH_2NH_3)_2CuCl_4$[70] ($|\Delta S_M| \approx 2$ J kg^{-1} K^{-1} at 17 K), $(PMA)_2CuCl_4$[71] ($|\Delta S_M| \approx 2.9$ J kg^{-1} K^{-1} at 20 K), and I^1O^2-CoC_{10}[72] ($|\Delta S_M| \approx 2.4$ J kg^{-1} K^{-1} at 11 K). Furthermore, the Mo (poly)oxometallates intercalation strengthens superexchange interactions compared with the chloride analog (α-$Co(OH)_2$), effectively adjusting the operating temperature toward the liquid hydrogen range (20–30 K). This is conducive to filling a critical gap in magnetocaloric materials, as few systems can achieve both large entropy changes and structural stability simultaneously. Our findings, therefore, highlight that strategic anion substitution in layered hydroxides can enhance the magnetocaloric response, offering a sustainable alternative to existing cryogenic refrigerants.

3. Conclusion

In conclusion, we have successfully synthesized 2D Co-based LDH nanosheets containing Mo using solvothermal conditions at 130 °C until a Co: Mo = 1:0.4 ratio. The ensemble of diffractometric and spectroscopic techniques allows us to prove that (poly)oxometallate specimens, based on MoO_6 octahedra, substitute Cl in the α-$Co(OH)_2$ phase resulting in bulky Mo interleaved specimens in the Co hydroxide nanolayers in a similar fashion to that observed in the α-$Co(OH)_2$ simonkolleite phase. Conventional XRD indicates, in agreement to previous reports, the expansion of the interlayered space. However, short-range order characterization through synchrotron and subsequent PDF analysis sheds light on the nature of the molybdenum (poly)oxometallate suggesting the local presence of edge-sharing MoO_6 octahedra, connected to the Co hydroxide layers via corner-sharing coordination. HRTEM locally confirms the expansion

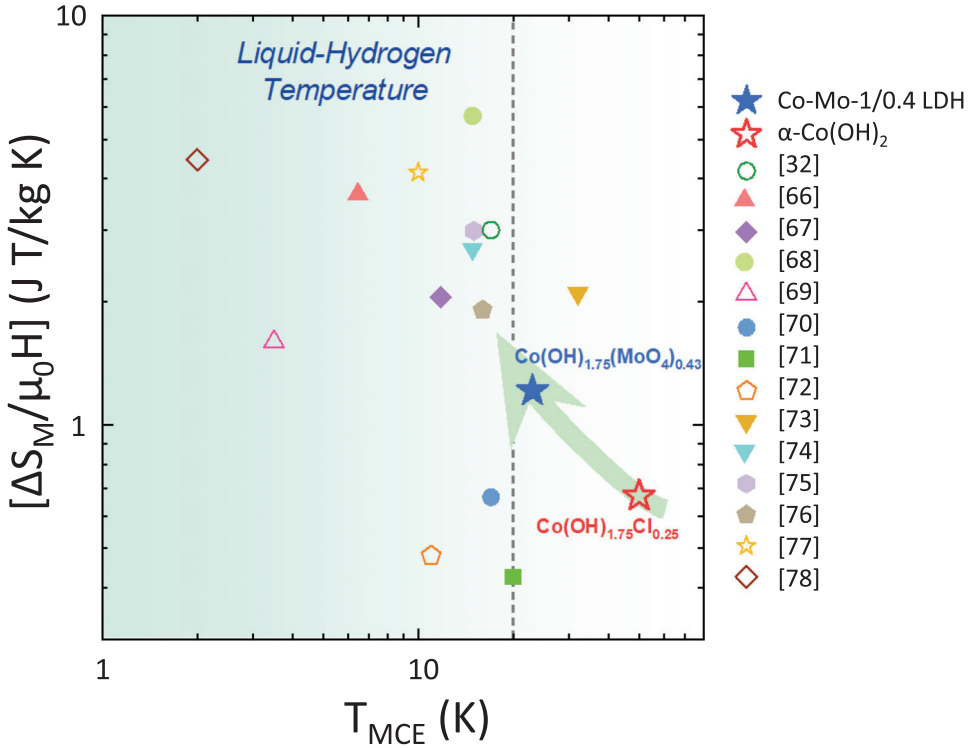

Figure 9. Comparative magnetic entropy changes normalized by the applied magnetic field ($\Delta S_M/\mu_0 H$), as a function of the MCE peak temperature (T_{MCE}) α-$Co(OH)_2$ and Co-Mo-1/0.4 LDH compounds with other reported prospective magnetocaloric materials.[32,66–78]

of layered compounds, while STEM-HAADF-EELS suggests the presence of Mo in the interlayered space. XAS and EELS experiments confirm the presence of Co^{3+} in the Co-Mo-1/0.4 LDH sample, in agreement with the incorporation of the oxomolybdate. Synchrotron short-range order characterization and subsequent PDF analysis shed light on the nature of molybdenum (poly)oxometallates. Equally, XPS and EELS confirm the presence of Mo(VI) as expected for the molybdate specimen. The functional behavior of Co-Mo-1/0.4 LDH has been studied. On one side it exhibits a superior electrochemical behavior in the OER in comparison to RuO_2. On the other side, its magnetic behavior has been explored resulting in a promising material due to its magnetocaloric response at liquid H_2 temperature, that opens new expectations as an alternative to cryogenic refrigerants at liquid-hydrogen temperature based on the compositional and structural flexibility of the Co-Mo LDH system.

4. Experimental Section

Synthesis: A sample consisting in a layered/ultrathin/$Co(OH)_2$ interleaved with Mo-based oxometallates, with a Co: Mo ratio 1/0.4 (Co-Mo-1/0.4 LDH) was prepared in a one-pot polyol synthesis based on a previous work reported elsewhere.[15] $CoCl_2.6H_2O$ and $Na_2MoO_4.4H_2O$ precursors were dissolved in ethylene glycol (1.5 M) and then, NH_3 (5 M) was slowly added until the pH was adjusted to 9.5. The resulting solution was placed in a Teflon-lined stainless-steel container, heated up at 130 °C for 24 h and then cooled down to room temperature. The obtained colloidal precipitate was sonicated for 6 h to favor layer separation. The resulting dispersion was centrifuged at 4000 rpm for 5 min, and the as-obtained solid was washed with water at 21 000 rpm for 5 min until pH = 7. An identical process was carried out to obtain the pristine α-$Co(OH)_2$ (Mo free). A sample with lower Mo content (Co-Mo-1/0.1 LDH), was also prepared for comparison purposes.

Compositional and Structural Characterization: All solids were characterized by powder XRD using a Bruker D8-ADVANCE A25 diffractometer with a Bragg–Brentano geometry. Additional experiments were carried out using a Panalytical Multi-Purpose Diffractometer Model Empyrean. Average cation composition was determined by means of EPMA. FTIR measurements were carried out in the 4000–650 cm^{-1} spectral range with a Perkin–Elmer Spectrum 100 equipped with a universal ATR accessory.

Total scattering X-ray data were collected at ESRF (beamline ID5A, beamtime MA-6541) operating at 65.34 keV (0.18972 Å). Additional data were collected at Diamond Light Source, UK (beamline I15-1, beamtime CY40307-1) operating at 76.69 KeV (λ = 0.161669 Å). All powder samples were ground and loaded into kapton capillaries (1 mm diameter) and sealed with plasticine. Total scattering data were collected at room temperature for the background (i.e., empty instrument), empty kapton capillary, and all the samples. Data were processed in both cases using GudrunX following well-documented procedures.[79,80]

X-ray absorption spectroscopy (XAS) was used for the determination of the average oxidation state of Co by measuring its L_3- L_2- absorption edges at the VerSox B07 beamline at Diamond Light Source.[81]

To gain further inside in the Co and Mo electronic states, X-ray photoelectron spectroscopy (XPS) analyses were performed using a SPECS GmbH spectrometer equipped with a PHOIBOS 150 MCD-9 detector and a non-monochromatic Mg Kα radiation source (200 W, 12 kV). Data processing was carried out using XPSPEAK software, and the binding energy values were calibrated with respect to the adventitious carbon C 1s peak.

A more detailed morphological and microstructural study of the layered systems was performed by transmission electron microscopy (TEM) in JEOL JEM 2100 and image aberration corrector JEOL JEM GRAND ARM300cF electron microscopes operating at 200 and 120 kV, respectively. Both microscopes were fitted with energy dispersive spectrometers (EDS)

allowing a more local compositional characterization. Additionally, the Co and Mo distribution as well their oxidation states were studied by STEM-HAADF-EELS on a probe-corrected aberration microscope JEOL JEM ARM 200cF operating at 120 kV. Low voltages and electron doses were employed to minimize sample damage. High-angle annular dark field (HAADF) images were acquired at 68–280 mrad inner and outer collection semi-angles. EELS experiments were acquired using a GIF-QuantumER with collection and convergence semiangles of 18 and 20.3 mrad, respectively. The dual EELS function of the GIF-QuantumER spectrometer was used to record simultaneously zero-loss peaks and core regions in order to minimize the uncertainty on the energy shift. EEL spectra were acquired by using spectrum line mode, with 0.25 energy dispersion per channel, an acquisition time of 0.5 s over an average total number of 100–150 points per particle, in a total of 100 particles per composition, and a pixel size of ≈2 Å. EELS spectrum lines were acquired scanning the beam over a line in the particles during short times to minimize sample damage. Principal component analysis was performed on the EELS data set to de-noise the spectra by using the MSA (multivariate statistical analysis) plugins for the GatanDMS analysis toolbox.51. Transition metal oxidation states were analyzed from electron loss near energy edge structure of Co-$L_{2,3}$ and Mo-$M_{2,3}$ edges. Numerical values of Co oxidation state were estimated by $-L_{2,3}$ interpolation in the fitting curves reported by Wang et al.[82] and error bars by repeating the $L_{2,3}$ calculation, modifying the integrate window position ±1 pixel.

Electrochemical Characterization: The electrochemical properties of the prepared hydroxides were tested by conventional three electrode setup using catalyst inks prepared by mixing the sample powders (8 mg) with Vulcan XC-72R (2 mg) carbon black and grounded with a drop of isopropyl alcohol and then transferred to a vail with 1.5 mL of isopropyl alcohol and 0.5 mL of distilled water mixture (3:1 vol. ratio), to which 40 µL of Nafion 1100 EW 5 wt.% dispersion was added as a binder. This mixture was sonicated for 30 min until a homogeneous slurry was obtained. Afterward, 6 µL of this ink was dropped on the surface of a polished glassy carbon rotating disk electrode of 5 mm in diameter (Pine, RDE), and dried at room temperature for 60 min to obtain a thin film with a catalyst loading of 0.2 mg cm^{-2}. Similarly, the OER control RuO_2 was prepared by loading 0.2 mg cm^{-2} of the pure oxide. Linear sweep voltammetry was carried out at room temperature using a Gamry potentiostat model Interface 5000E. The voltammograms were recorded in 0.5 M aqueous KOH electrolyte saturated with oxygen, and using a Pt wire as a counter electrode, and Ag/AgCl with 3.5 M KCl as a reference electrode.

Magnetic Characterization: The magnetic properties were measured using a Squid magnetometer from QD (San Diego, USA), model MPMS-3S. The temperature range available was from 1.8 till 400 K and the magnetic field covering up to 7 T (bipolar). In the case of *ac* magnetic susceptibility measurements, the frequency range explored went from 0.1 Hz till 1 kHz, using a modulated magnetic field with an amplitude of 1 Oe.

Supporting Information

Supporting Information is available from the Wiley Online Library or from the author.

Acknowledgements

The authors acknowledge support from the: "(MAD2D-CM)-UCM project funded by the Comunidad de Madrid PR47/21 MAD2D-CM PRTR-CM (CM) UCM6; by the Recovery, Transformation and Resilience Plan; and by the NextGenerationEU from the European Union"; "Spanish Ministry for Science, Innovation and Universities" (MICIU/AEI/10.13039/501 100 011 033), European Union "NextGenerationEU/PRTR and ERDF with grant numbers: PID2021-122477OB- I00, PID2021-123287OB-I00, TED2021-129254B–C21, TED2021-129254B–C22, also GREHENER (Green Hydrogen Production with Next Generation Polymeric Electrolyzers) project TED2022-131033B-100";"Spanish Ministerio de Economía y Competitividad, the Ministerio de Ciencia e Innovación, la Agencia Estatal de Investigaci"ón, MCIN/AEI/10.13039/501 100 011 033/FEDER UE, and the European Union "NextGenerationEU"/PRTR (PID2022-140370NB-I00, RYC2021-033764-I, CPP2021-008986, CNS2024-154587". C.C.-B. gratefully acknowledges Comunidad de Madrid for an Atracción de Talento César Nombela grant (2024-T1/TEC-31450). Authors thank ESRF (ID15A, MA-4561) and Diamond Light Source (Instrument B07-B/VerSoX and the Harwell XPS facility, proposal SI40403-1) for synchrotron access. Drs. A. Azor and M. Cabero (ICTS ELECMI-CNME (UCM)) and Prof. J. J. Calvino (Universidad de Cádiz) are acknowledged for fruitful discussions.

Conflict of Interest

The authors declare no conflict of interest.

Data Availability Statement

The data that support the findings of this study are available from the corresponding author upon reasonable request.;

Keywords

2D transition metal oxides, double layers hydroxides, magnetocaloric effect, oxygen evolution reaction (OER), pair distribution function (PDF)

Received: June 30, 2025
Revised: September 24, 2025
Published online:

[1] S. Kumar, R. Muhammad, S. Kim, J. Yi, K. Son, H. Oh, *Adv. Funct. Mater.* **2024**, *34*, 2402513.
[2] A. Gschneidner, V. K. Pecharsky, A. O. Tsokol, *Rep. Prog. Phys.* **2005**, *68*, 1479.
[3] R. S. Silva, J. Gainza, C. dos Santos, J. E. F. S. Rodrigues, C. Dejoie, Y. Huttel, N. Biskup, N. M. Nemes, J. L. Martínez, N. S. Ferreira, J. A. Alonso, *Chem. Mater.* **2023**, *35*, 2439.
[4] O. Gutfleisch, M. A. Willard, E. Brück, C. H. Chen, S. G. Sankar, J. P. Liu, *Adv. Mater.* **2011**, *23*, 821.
[5] V. K. Pecharsky, K. A. Gschneidner, *Phys. Rev. Lett.* **1997**, *78*, 4494.
[6] A. Zeleňáková, P. Hrubovčák, A. Berkutova, O. Šofranko, N. Kučerka, O. Ivankov, A. Kuklin, V. Girman, V. Zeleňák, *Sci. Rep.* **2022**, *12*, 2282.
[7] B. Zhang, J. Zhang, X. Tan, D. Tan, J. Shi, F. Zhang, L. Liu, Z. Su, B. Han, L. Zheng, J. Zhang, *Chem. Commun.* **2018**, *54*, 4045.
[8] F. C. Hawthorne, E. Sokolova, *Can. Mineral.* **2002**, *40*, 939.
[9] R. Ma, Z. Liu, K. Takada, K. Fukuda, Y. Ebina, Y. Bando, T. Sasaki, *Inorg. Chem.* **2006**, *45*, 3964.
[10] R. Ma, K. Takada, K. Fukuda, N. Iyi, Y. Bando, T. Sasaki, *Angew. Chem., Int. Ed.* **2008**, *47*, 86.
[11] R. Sanchis-Gual, D. Hunt, C. Jaramillo-Hernández, A. Seijas-Da Silva, M. Mizrahi, C. Marini, V. Oestreicher, G. Abellán, *ACS Catal.* **2023**, *13*, 10351.
[12] F. Lyu, Y. Bai, Q. Wang, L. Wang, X. Zhang, Y. Yin, *Dalton Trans.* **2017**, *46*, 10545.
[13] A. H. Dorrah, J.-S. Park, A. Palmieri, F. Capasso, *Nat. Commun.* **2024**, *16*, 3126.
[14] H. Hu, B. Y. Guan, X. W. (David) Lou, *Chem* **2016**, *1*, 102.
[15] J. Huang, J. Chen, T. Yao, J. He, S. Jiang, Z. Sun, Q. Liu, W. Cheng, F. Hu, Y. Jiang, Z. Pan, S. Wei, *Angew. Chem., Int. Ed.* **2015**, *54*, 8722.
[16] L. Tang, L. Yu, C. Ma, Y. Song, Y. Tu, Y. Zhang, X. Bo, D. Deng, *J. Mater. Chem. A* **2022**, *10*, 6242.
[17] F. Fievet, S. Ammar-Merah, R. Brayner, F. Chau, M. Giraud, F. Mammeri, J. Peron, J. Y. Piquemal, L. Sicard, G. Viau, *Chem. Soc. Rev.* **2018**, *47*, 5187.

[18] Z. A. Hu, Y. L. Xie, Y. X. Wang, L. J. Xie, G. R. Fu, X. Q. Jin, Z. Y. Zhang, Y. Y. Yang, H. Y. Wu, *J. Phys. Chem. C* **2009**, *113*, 12502.
[19] L. N. Zhang, G. A. Jia, C. Ma, M. Q. Jia, T. S. Li, L. Bin Ni, G. W. Diao, *Inorg. Chem.* **2024**, *63*, 6787.
[20] J. Soriano-López, J. Quirós-Huerta, Á. Seijas-Da Silva, R. Torres-Cavanillas, E. Andres-Garcia, G. Abellán, E. Coronado, *Inorg. Chem.* **2025**, *64*, 3242.
[21] X. Zhang, H. Zhong, Q. Zhang, Q. Zhang, C. Wu, J. Yu, Y. Ma, H. An, H. Wang, Y. Zou, C. Diao, J. Chen, Z. G. Yu, S. Xi, X. Wang, J. Xue, *Nat. Commun.* **2024**, *15*, 1383.
[22] J. Suntivich, H. A. Gasteiger, N. Yabuuchi, H. Nakanishi, J. B. Goodenough, Y. Shao-Horn, *Nat. Chem.* **2011**, *3*, 546.
[23] Y. Zheng, R. Gao, Y. Qiu, L. Zheng, Z. Hu, X. Liu, *Inorg. Chem.* **2021**, *60*, 5252.
[24] B. Zhang, X. Zheng, O. Voznyy, R. Comin, M. Bajdich, M. García-Melchor, L. Han, J. Xu, M. Liu, L. Zheng, F. Pelayo García De Arquer, C. T. Dinh, F. Fan, M. Yuan, E. Yassitepe, N. Chen, T. Regier, P. Liu, Y. Li, P. De Luna, A. Janmohamed, H. L. Xin, H. Yang, A. Vojvodic, E. H. Sargent, *Science* **2016**, *352*, 333.
[25] A. Grimaud, W. T. Hong, Y. Shao-Horn, J. M. Tarascon, *Nat. Mater.* **2016**, *15*, 121.
[26] J. Bai, J. Mei, T. Liao, Q. Sun, Z. G. Chen, Z. Sun, *Adv. Energy Mater.* **2022**, *12*, 2103247.
[27] X. Zhu, J. Lyu, S. Wang, X. Li, X. Wei, C. Chen, W. Kooamornpattana, F. Verpoort, J. Wu, Z. Kou, *Nano Res.* **2024**, *17*, 5080.
[28] Y. L. Meng, Y. Li, Z. Tan, X. Chen, L. L. Wu, L. W. Ji, Q. S. Wang, X. Z. Song, S. Song, *Energy Fuels* **2021**, *35*, 2775.
[29] Z. Guo, Y. He, P. Chen, R. Li, Z. Wang, X. Xu, S. Chang, Y. Li, R. Jia, S. Han, *Int. J. Hydrogen Energy* **2024**, *92*, 1500.
[30] C. Vaysse, L. Guerlou-Demourgues, A. Demourgues, F. Lazartigues, D. Fertier, C. Delmas, *J. Mater. Chem.* **2002**, *12*, 1035.
[31] A. Davantès, G. Lefèvre, *J. Phys. Chem. A* **2013**, *117*, 12922.
[32] J. J. B. Levinsky, B. Beckmann, T. Gottschall, D. Koch, M. Ahmadi, O. Gutfleisch, G. R. Blake, *Nat. Commun.* **2024**, *15*, 8559.
[33] G. Abellán, C. Martí-Gastaldo, A. Ribera, E. Coronado, *Acc. Chem. Res.* **2015**, *48*, 1601.
[34] J. A. Carrasco, V. Oestreicher, A. S. Da Silva, G. Abellán, *Appl. Clay Sci.* **2023**, *243*, 107073.
[35] Z. Liu, R. Ma, M. Osada, K. Takada, T. Sasaki, *J. Am. Chem. Soc.* **2005**, *127*, 13869.
[36] C. Castillo-Blas, I. Romero-Muñiz, A. Mavrandonakis, L. Simonelli, A. E. Platero-Prats, *Chem. Commun.* **2020**, *56*, 15615.
[37] F. Steffler, G. F. de Lima, H. A. Duarte, *Chem. Phys. Lett.* **2017**, *669*, 104.
[38] D. K. Bora, X. Cheng, M. Kapilashrami, P. A. Glans, Y. Luo, J. H. Guo, *J. Synchrotron Radiat.* **2015**, *22*, 1450.
[39] T. J. Park, S. Sambasivan, D. A. Fischer, W. S. Yoon, J. A. Misewich, S. S. Wong, *J. Phys. Chem. C* **2008**, *112*, 10359.
[40] W. Jauch, M. Reehuis, H. J. Bleif, F. Kubanek, P. Pattison, *Phys. Rev. B* **2001**, *64*, 052102.
[41] M. Rogala, S. Sokołowski, U. Ukegbu, A. Mierzwa, R. Szoszkiewicz, *Adv. Mater. Interfaces* **2021**, *8*, 202100328.
[42] F. Xie, W. C. H. Choy, C. Wang, X. Li, S. Zhang, J. Hou, *Adv. Mater.* **2013**, *25*, 2051.
[43] T. Zhou, Z. Cao, H. Wang, Z. Gao, L. Li, H. Ma, Y. Zhao, *RSC Adv.* **2017**, *7*, 22818.
[44] Y. Yang, X. Yuan, Q. Wang, S. Wan, C. Lin, S. Lu, Q. Zhong, K. Zhang, *Angew. Chem., Int. Ed.* **2024**, *63*, 202314383.
[45] L. Zhuang, Y. Jia, T. He, A. Du, X. Yan, L. Ge, Z. Zhu, X. Yao, *Nano Res.* **2018**, *11*, 3509.
[46] S. Khan, E. S. Y. Aw, L. A. V. Nagle-Cocco, A. Sud, S. Ghosh, M. K. B. Subhan, Z. Xue, C. Freeman, D. Sagkovits, A. Gutiérrez-Llorente, I. Verzhbitskiy, D. M. Arroo, C. W. Zollitsch, G. Eda, E. J. G. Santos, S. E. Dutton, S. T. Bramwell, C. A. Howard, H. Kurebayashi, *Adv. Mater.* **2024**, *36*, 202400270.
[47] Q. Yang, D. Wang, C. Wang, X. Li, K. Li, Y. Peng, J. Li, *Catal. Sci. Technol.* **2018**, *8*, 3166.
[48] Q. Wang, L. Ma, *New J. Chem.* **2019**, *43*, 2974.
[49] X. Wei, Y. Chai, W. Chen, N. Liu, S. Qiao, *Ionics* **2022**, *28*, 3945.
[50] L. Lajaunie, F. Boucher, R. Dessapt, P. Moreau, *Ultramicroscopy* **2015**, *149*, 1.
[51] Y. Jiang, X. Li, T. Wang, C. Wang, *Nanoscale* **2016**, *8*, 9667.
[52] S. Cheng, K. Du, X. Wang, Y. Han, L. Li, G. Wen, *Nanomaterials* **2023**, *13*, 2663.
[53] P. Li, Z. Zhuang, C. Du, D. Xiang, F. Zheng, Z. Zhang, Z. Fang, J. Guo, S. Zhu, W. Chen, *ACS Appl. Mater. Interfaces* **2020**, *12*, 40194.
[54] O. van der Heijden, S. Park, R. E. Vos, J. J. J. Eggebeen, M. T. M. Koper, *ACS Energy Lett.* **2024**, *9*, 1871.
[55] Z. Bai, R. Guo, J. Kuang, H. Chen, W. Sha, A. Xie, J. Liu, P. Wan, Y. Tang, *Nanoscale* **2025**, *17*, 17529.
[56] B. C. Zhao, Y. P. Sun, S. B. Zhang, W. H. Song, J. M. Dai, *J. Appl. Phys.* **2007**, *102*, 113903.
[57] S. Mugiraneza, A. M. Hallas, *Commun. Phys.* **2022**, *5*, 95.
[58] K. Binder, A. P. Young, C. D. F. Gen, *Rev. Mod. Phys.* **1986**, *58*, 801.
[59] R. S. Silva, J. Gainza, J. E. Rodrigues, L. Martínez, E. Céspedes, N. M. Nemes, J. L. Martínez, J. A. Alonso, *J. Mater. Chem. C Mater.* **2022**, *10*, 15929.
[60] H. Sun, L. Tian, J. Gong, Z. Li, Z. Mo, G. Liu, J. Shen, *APL Energy* **2025**, *3*, 026103.
[61] V. Franco, J. S. Blázquez, J. J. Ipus, J. Y. Law, L. M. Moreno-Ramírez, A. Conde, *Prog. Mater. Sci.* **2018**, *93*, 112.
[62] R. S. Silva, C. Santos, M. T. Escote, B. F. O. Costa, N. O. Moreno, S. P. A. Paz, R. S. Angélica, N. S. Ferreira, *Phys. Rev. B 106*, 134439.
[63] V. Provenzano, A. J. Saphiro, R. D. Shull, *Nature* **2004**, *429*, 853.
[64] T. Toliński, M. Falkowski, K. Synoradzki, A. Hoser, N. Stüßer, *J. Alloys Compd.* **2012**, *523*, 43.
[65] M. Halder, S. M. Yusuf, M. D. Mukadam, K. Shashikala, *Phys. Rev. B* **2010**, *81*, 174402.
[66] X. Zheng, B. Zhang, Y. Li, H. Wu, H. Zhang, J. Zhang, S. Wang, Q. Huang, B. Shen, *J. Alloys Compd.* **2016**, *680*, 617.
[67] X. Q. Zheng, J. W. Xu, H. Zhang, J. Y. Zhang, S. G. Wang, Y. Zhang, Z. Y. Xu, L. C. Wang, B. G. Shen, *AIP Adv.* **2018**, *8*, 056432.
[68] L. Meng, C. Xu, Y. Yuan, Y. Qi, S. Zhou, L. Li, *RSC Adv.* **2016**, *6*, 74765.
[69] P. Danylchenko, R. Tarasenko, E. Čižmár, V. Tkáč, A. Uhrinová, A. Orendáčová, M. Orendáč, *Magnetochemistry* **2022**, *8*, 106.
[70] G. Park, J. Cho, J. S. Kim, Y. Kim, J. H. Jung, N. Hur, I. H. Oh, K. Y. Kim, *Curr. Appl. Phys.* **2022**, *35*, 24.
[71] L. Septiany, G. R. Blake, *J. Magn. Magn. Mater.* **2022**, *542*, 168598.
[72] R. Sibille, T. Mazet, B. Malaman, T. Gaudisson, M. François, *Inorg. Chem.* **2012**, *51*, 2885.
[73] X. Liu, C. Feng, F. Xiao, S. W. Or, Y. Sun, C. Jin, A. Xia, *Mater. Res.* **2014**, *17*, 186.
[74] X. H. Liu, W. Liu, W. J. Hu, S. Guo, X. K. Lv, W. B. Cui, X. G. Zhao, Z. D. Zhang, *Appl. Phys. Lett.* **2008**, *93*, 202502.
[75] W. Wei, R. K. Xie, S. W. Du, C. Bin Tian, G. L. Chai, *J. Alloys Compd.* **2021**, *878*, 160353.
[76] S. H. Song, J. A. Alonso, M. T. Fernández-Díaz, S. H. Lim, *Eur. J. Inorg. Chem.* **2017**, *2017*, 2289.
[77] N. F. Li, Y. T. Yu, Q. Wang, Y. Xu, *J. Mol. Struct.* **2024**, *1315*, 138844.
[78] H. Wada, Y. Tanabe, M. Shiga, H. Sugawara, H. Sato, *J. Alloys Compd.* **2001**, *316*, 245.

[79] A. K. Soper, E. R. Barney, *J. Appl. Crystallogr.* **2011**, *44*, 714.
[80] D. A. Keen, *J. Appl. Cryst.* **2001**, *34*, 172.
[81] D. C. Grinter, P. Ferrer, F. Venturini, M. A. van Spronsen, A. I. Large, S. Kumar, M. Jaugstetter, A. Iordachescu, A. Watts, S. L. M. Schroeder, A. Kroner, F. Grillo, S. M. Francis, P. B. Webb, M. Hand, A. Walters, M. Hillman, G. Held, *J. Synchrotron Radiat.* **2024**, *31*, 578.
[82] Z. L. Wang, J. S. Yin, Y. D. Jiang, *Micron* **2000**, *31*, 571.